Nano Energy 53 (2018) 91–96

Contents lists available at ScienceDirect

Nano Energy

journal homepage: www.elsevier.com/locate/nanoen

Full paper

Ultrahigh rate capability and ultralong cycling stability of sodium-ion batteries enabled by wrinkled black titania nanosheets with abundant oxygen vacancies

Lianbo Ma[a], Xin Gao[a], Wenjun Zhang[a], Hao Yuan[a], Yi Hu[a], Guoyin Zhu[a], Renpeng Chen[a], Tao Chen[a], Zuoxiu Tie[a,*], Jie Liu[a,b,**], Tom Wu[c], Zhong Jin[a,*]

[a] Key Laboratory of Mesoscopic Chemistry of MOE, School of Chemistry and Chemical Engineering, Nanjing University, Nanjing, Jiangsu 210023, China
[b] Department of Chemistry, Duke University, Durham, NC 27708, USA
[c] Physical Science and Engineering Division, King Abdullah University of Science & Technology (KAUST), Thuwal 23955-6900, Saudi Arabia

ARTICLE INFO

Keywords:
Sodium-ion batteries
Wrinkled TiO_{2-x} nanosheets with oxygen vacancies
Conductive networks
Rate capability
Cycling stability

ABSTRACT

Sodium-ion batteries (SIBs) have been considered as one of the promising alternatives for lithium-ion batteries, owning to the abundant reserve and low cost of sodium-related salts. However, SIBs usually suffer from the sluggish kinetics of Na^+ and the serious volume expansion of anode materials, which inevitably restrict the performance of SIBs. Herein, electroconductive wrinkled anatase-phase black titanium oxide nanosheets with rich oxygen vacancies (*OVs*-TiO_{2-x}) was found to have an ultrafast Na^+ insertion and extraction kinetics as anode material in SIBs. The wrinkled structure can significantly reduce the Na^+ diffusion length, and the conductive networks formed by wrinkled *OVs*-TiO_{2-x} can boost the electron transfer during Na^+ insertion and extraction processes. With the rapid Na^+ insertion/extraction ability, wrinkled *OVs*-TiO_{2-x} delivers excellent sodium storage performance with high reversible capacity, ultra-high rate capability with the capacity reaches 91 mAh g^{-1} even at 20,000 mA g^{-1}, and ultra-long cycling stability. These properties demonstrated the great potential of wrinkled *OVs*-TiO_{2-x} to serve as a realistic choice of anode materials in SIBs.

1. Introduction

Sodium-ion batteries (SIBs) have been regarded as one of the potential choices to partially replace conventional lithium-ion batteries (LIBs), because of the abundant nature and low costs of elemental sodium and sodium-related salts [1–4]. Nevertheless, owning to the large radium of Na^+ (0.97 Å, ~ 55% larger than that of Li^+), the commercialization of SIBs is seriously hindered by the sluggish kinetics of Na^+ and the serious volume expansion and even structural collapse of host material upon Na^+ insertion/extraction [5–10], which inevitably deteriorate the performance of SIBs. To alleviate the above issues, materials based on redox conversion and alloy reactions [11–15] and hard carbonaceous materials [16–18], have been developed as the anode for SIBs. Unfortunately, these electrodes still suffer from the inferior long-term cycling stability and/or poor rate capability under high rates [19–21].

With impressive cycle stability and high rate capability as anode material in LIBs [22–24], titanium dioxide (TiO_2), a stable, reserve abundant, nontoxic and low-cost material, has been recently considered as the potential anodes for SIBs [25]. By date, micro/nanostructured TiO_2 [26–29] and TiO_2/carbon hybrids [30] have been investigated, and the achieved SIBs demonstrated good rate performance and long cycling life. It was expected that the sodium storage performance of TiO_2 could be significantly improved through the partial reduction of Ti^{4+} to Ti^{3+} [16,31]. A simple and effective way is to introduce Ti^{3+} species into the TiO_2 structures, so that the mix-valence states can help to improve the electronic conductivity of TiO_2 [32–34]. However, the existing methods for introducing Ti^{3+} species are usually complicate, and the synthesis processes may involve high pressure, high reaction temperature (> 600 °C), dangerous combustive reductants (e.g. Mg, Al, Zn, $NaBH_4$ and CaH_2), and strongly exothermic reactions [35,36], which inevitably hamper the extensive applications. More importantly, the contents of Ti^{3+} introduced by those methods are usually very limited. Thus, it is challenging and crucial to design novel strategies for

* Corresponding authors.
** Corresponding author at: Key Laboratory of Mesoscopic Chemistry of MOE, School of Chemistry and Chemical Engineering, Nanjing University, Nanjing, Jiangsu 210023, China.
E-mail addresses: zxtie@nju.edu.cn (Z. Tie), j.liu@duke.edu (J. Liu), zhongjin@nju.edu.cn (Z. Jin).

https://doi.org/10.1016/j.nanoen.2018.08.043
Received 17 March 2018; Received in revised form 6 August 2018; Accepted 20 August 2018
Available online 21 August 2018

preparing Ti^{3+}-rich TiO_2 nanostructures with adjustable atomic structure and improved electrochemical performances.

Herein, we report that wrinkled *OVs*-TiO_{2-x} with rich electro-conducting Ti^{3+} species can exhibit remarkable electrochemical performances as a superior anode material for sodium storage. The square planar sites at the center of distorted octahedral positions in *OVs*-TiO_{2-x} are thermodynamically and energetically favorable for the Na^+ intercalation. Theoretically, two Na^+ ions can be inserted into a single unit cell of *OVs*-TiO_{2-x}. As measured by four-point probe method, the wrinkled *OVs*-TiO_{2-x} nanosheets with rich oxygen vacancies have much higher electrical conductivity ($0.041\ S\ m^{-1}$) than pristine TiO_2 ($0.008\ S\ m^{-1}$). Moreover, the wrinkled *OVs*-TiO_{2-x} nanosheets possess lower sodiation energy barrier and higher activity towards Na^+ insertion/extraction [25,37]. Benefited from the well-designed wrinkled structure, *OVs*-TiO_{2-x} exhibits greatly reduced diffusion length of Na^+. Furthermore, the wrinkled *OVs*-TiO_{2-x} stacked and twined together to form a three-dimensional interconnected structure, which can serve as an unobstructed electroconductive network. In result, the wrinkled *OVs*-TiO_{2-x} based anode exhibit impressive rate capability and ultralong cycling stability, demonstrating very remarkable sodium storage performance among existing TiO_2 materials.

2. Experimental

2.1. Synthesis of TiO_2 nanosheets

In a typical synthesis, 10 mL of tetrabutyl titanate and 1.5 mL of hydrofluoric acid (HF, 40.0 wt%) solution were mixed together and further stirred at 0 °C for 3 h. Then, the mixture was transferred into an autoclave and heated at 180 °C for 24 h. After cooling down to room temperature naturally, the precipitate was collected, washed with deionized water and absolute ethanol, and dried under vacuum at 50 °C overnight. Finally, the powder was further annealed at 600 °C for 3 h at a ramping rate of $2\ °C\ min^{-1}$.

2.2. Synthesis of wrinkled TiO_2 and OVs-TiO_{2-x}

Typically, 400 mg of TiO_2 nanosheets was dispersed into a 40 mL of deionized water containing 16 g of NaOH under vigorous stirring. Subsequently, the mixture was transferred into an autoclave and heated at 140 °C for 2 h. Then, the precipitate ($Na_2Ti_3O_7$) was collected, ion exchanged by a HCl aqueous solution, washed with deionized water and dried under vacuum at 60 °C for 12 h. Finally, the above powder was annealed at 500 °C for 6 h under air with the ramping rate of $2\ °C\ min^{-1}$ to obtain wrinkled TiO_2. In order to achieve wrinkled *OVs*-TiO_{2-x}, the wrinkled TiO_2 were further annealed at 500 °C for 4 h under H_2 atmosphere with the same heating rate.

2.3. Instruments and Characterizations

Scanning electron microscopy (SEM) images were collected on a JEOL JSM-6480 instrument. Transmission electron microscopy (TEM, JEM-2100) images were taken on a JEOL JEM-2100F using an accelerating voltage of 200 kV. The powder X-ray diffraction (XRD) patterns were recorded with an X-ray diffractometer (Bruker D-8 Advance) using Cu Kα (λ = 1.5406 Å) radiation at a scanning rate of $6°\ min^{-1}$. Raman analysis was performed on a Horiba JY Raman spectrometer using a 473 nm laser source. The diffuse reflectance UV–Vis spectra were collected on a Japan Shimadzu UV–Vis spectrophotometer (UV-2600) in the range of 200 − 800 nm. Nitrogen sorption isotherms were obtained through Brunauer–Emmett–Teller (BET) analysis at 77 K on a Quantachrome Autosorb-IQ-2C-TCD-VP instrument. EPR measurements were performed on a Bruker EMX-10/12 spectrometer equipped with a cylindrical cavity operating at a 100 kHz field modulation at 77 K. X-ray photoelectron spectra (XPS) were conducted on a PHI-5000 VersaProbe X-ray photoelectron spectrometer using an Al Kα X-ray radiation.

2.4. Electrochemical measurements

The working electrodes were prepared by mixing the selected samples, acetylene black and binder (polyvinylidene fluoride, PVDF) in N-methy-pyrrolidinone (NMP) solvent with a weight ratio of 80: 10: 10. The mixture was stirred for 24 h, spread on a carbon paper, and then dried in a vacuum oven at 60 °C to remove the solvent. The loading mass of active material in the electrodes is about 1.2–1.5 mg cm^{-2}. The SIBs were assembled in an argon-filled glovebox with the above-prepared anodes and sodium metal foil cathodes. The electrolyte was 1 M $NaClO_4$ in propylene carbonate (PC) with 5 vol% addition of fluoroethylene carbonate (FEC). The cycling performances of SIBs were measured on a LAND CT2001A analyzer at different current rates with a potential window of 0.01 − 2.5 V vs. Na/Na^+ under ambient temperature. The cyclic voltammograms (CV) curves were collected on a Chenhua CHI-760E electrochemical workstation at a scan rate of $0.2\ mV\ s^{-1}$ between 0.01–2.5 V *vs.* Na/Na^+. EIS analysis was carried

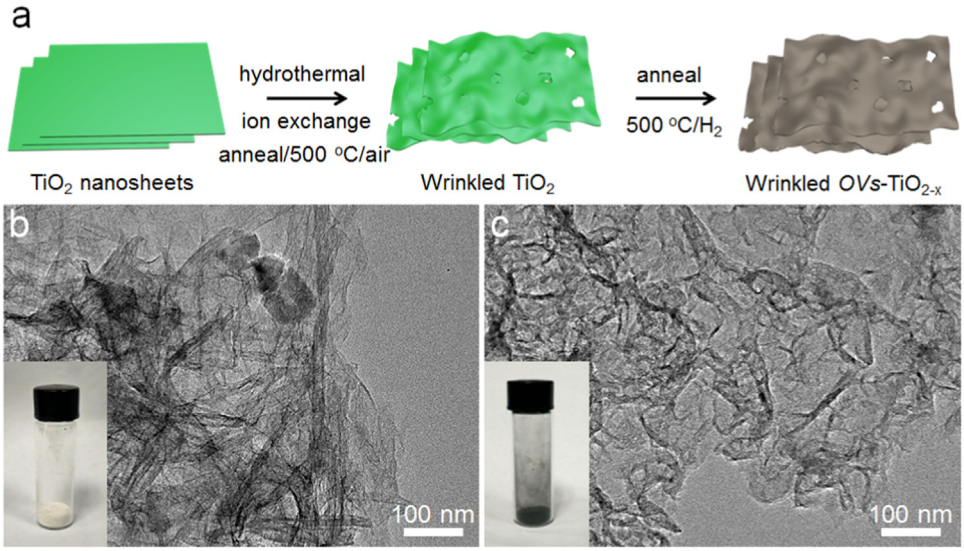

Fig. 1. Synthesis and morphology of wrinkled TiO_2 and *OVs*-TiO_{2-x}. (a) Schematic illustration of the synthesis of wrinkled TiO_2 and *OVs*-TiO_{2-x}. (b) TEM image of wrinkled TiO_2. (c) TEM image of wrinkled *OVs*-TiO_{2-x}. The insets in (b) and (c) are the photographs of wrinkled TiO_2 and *OVs*-TiO_{2-x}, respectively.

out in the range of 100 kHz to 0.01 Hz.

3. Results and discussions

As schematically illustrated in Fig. 1a, a two-step defect engineering strategy was developed to prepare *OVs*-TiO_{2-x}. Firstly, TiO_2 nanosheets were prepared through a hydrothermal method with tetrabutyl titanate as the starting material. X-ray diffraction (XRD) pattern (Fig. S1), scanning electron microscopy (SEM) and transmission electron microscopy (TEM) images (Fig. S2) confirm the preparation of anatase-phase TiO_2 nanosheets. The width of TiO_2 nanosheets reaches 2–3 μm, and the thickness is about several nanometers. Subsequently, through a hydrothermal method, TiO_2 nanosheets were converted to $Na_2Ti_3O_7$ in alkaline solution. After the following ion exchange and thermal annealing processes, TiO_2 nanosheets with wrinkled structures (wrinkled TiO_2) was prepared. Finally, wrinkled *OVs*-TiO_{2-x} nanosheets were obtained by heating the wrinkled TiO_2 under H_2 atmosphere. In this step, Ti^{4+} species were partially reduced to Ti^{3+} by H_2 treatment, resulting in the formation of Ti^{3+}-riched black titania with abundant oxygen vacancies. The colors of wrinkled TiO_2 and *OVs*-TiO_{2-x} are revealed by the photographs in the insets of Fig. 1b and c, respectively. SEM and TEM were conducted to examine the morphology and structural differences between TiO_2 and *OVs*-TiO_{2-x}. As shown in Fig. S3, the thickness of wrinkled *OVs*-TiO_{2-x} nanosheets is about several nanometers, comparable to that of wrinkled TiO_2. Fig. 1b presents the TEM image of wrinkled TiO_2, showing laminar morphology with crumple and wrinkle features. Moreover, as compared with pristine TiO_2 nanosheets, wrinkled TiO_2 shows numerous induced structural defects during the hydrothermal process under alkaline solution. After annealing under H_2 atmosphere, wrinkled *OVs*-TiO_{2-x}, as the final product, exhibit the morphology (Fig. 1c) similar to that of wrinkled TiO_2.

The crystalline structure of the samples was investigated by XRD (Fig. 2a). All the diffraction peaks can be well ascribed to the anatase TiO_2 (JCPDS card, No. 84-1285). The XRD pattern of wrinkled *OVs*-TiO_{2-x} shows broader peaks with weaker diffraction intensities than wrinkled TiO_2, which might be attributed to the disorder-induced lattice strains and reduced crystallite size resulted from the presence of oxygen vacancies [39]. The structural changes were further investigated by Raman spectroscopy (Fig. 2b). Four Raman peaks at 135, 387, 507 and 629 cm^{-1} were observed from wrinkled TiO_2, and could be assigned to the Raman bands of E_g, B_{1g}, A_{1g} and E_g of anatase TiO_2, respectively [40]. For wrinkled *OVs*-TiO_{2-x}, these peaks show obvious Raman shifting and broadening, indicating that the original symmetry of TiO_2 lattice was distorted due to the oxygen vacancies and disordered surface induced by the hydrogen annealing process [41,42]. Fig. S4 shows the UV–Vis spectra of both wrinkled TiO_2 and *OVs*-TiO_{2-x}. The wrinkled *OVs*-TiO_{2-x} displays a broad adsorption starting at ~ 400 nm and extending to the near-infrared region. Moreover, the adsorption band intensity of wrinkled *OVs*-TiO_{2-x} increased notably, in line with the color change of the samples. Furthermore, the presence of Ti^{3+} and H atoms was verified to influence the band structure of wrinkled *OVs*-TiO_{2-x} [32,38]. As indicated in Fig. 2c, the band gap energy of wrinkled TiO_2 was calculated to be 3.0 eV, comparable to that of normal TiO_2 material in literature [32]. While for wrinkled *OVs*-TiO_{2-x}, the band gap significantly decreased to ~ 1.1 eV, owing to the introduction of Ti^{3+} and H atoms. To evaluate the surface area and pore size characteristics of the samples, N_2 adsorption-desorption isotherms were measured (Fig. S5). The specific surface areas of wrinkled TiO_2 and *OVs*-TiO_{2-x} were measured to be 125.5 and 141.6 $m^2\ g^{-1}$, respectively, and the pore size distribution of wrinkled *OVs*-TiO_{2-x} are comparable to those of wrinkled TiO_2.

The surface compositions and chemical states were further examined by electron paramagnetic resonance (EPR) and X-ray photoelectron spectroscopy (XPS). The wrinkled TiO_2 shows almost no characteristic EPR response (Fig. 2d), whereas the wrinkled *OVs*-TiO_{2-x} present a distinct EPR signal with a *g* value of 1.964, indicating the existence of Ti^{3+} [43,44]. The survey XPS spectra of wrinkled TiO_2 and *OVs*-TiO_{2-x} are supplied in Fig. S6, revealing the co-existence of Ti and O elements. The high-resolution XPS spectra at Ti 2p regions were compared in Fig. 2e. For wrinkled TiO_2, the Ti $2p_{3/2}$ and Ti $2p_{1/2}$ peaks centered at binding energies of 463.9 and 458.1 eV are both the typical characteristics of Ti^{4+} [45]. While for wrinkled *OVs*-TiO_{2-x}, these two peaks down-shifted to lower binding energies of 463.4 and 458.0 eV, respectively, indicating the lower valence state of Ti species [46]. The

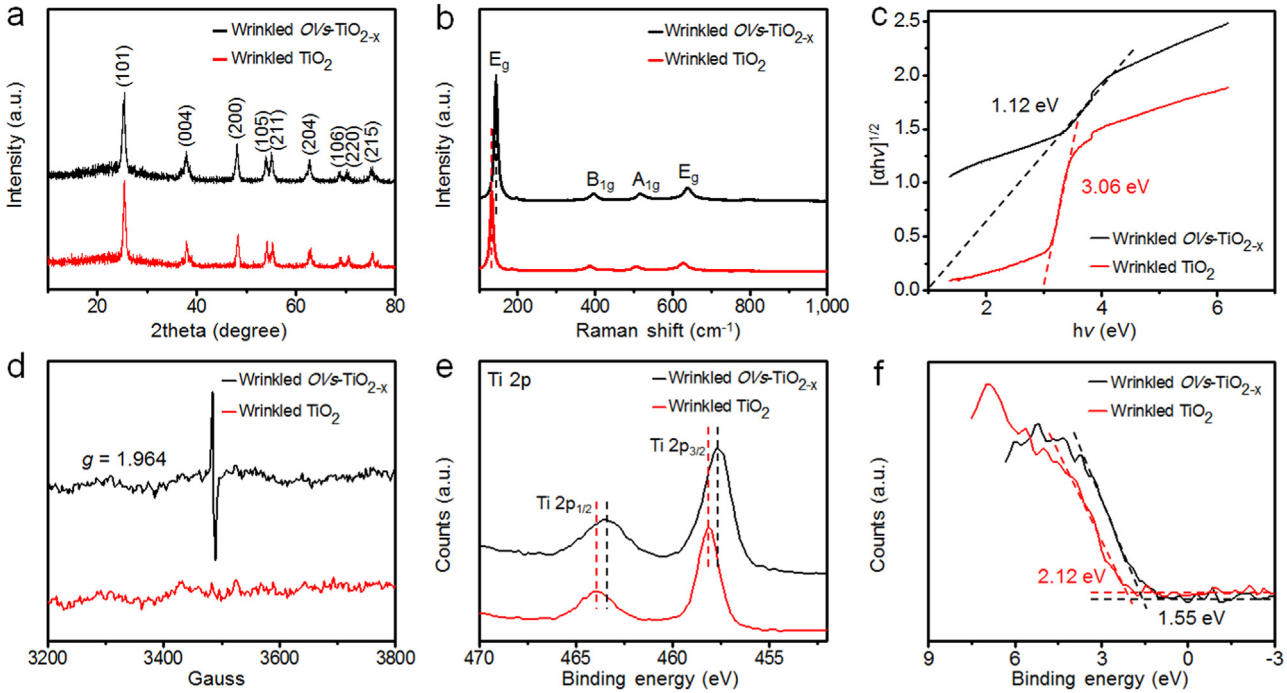

Fig. 2. Characterizations of wrinkled TiO_2 and *OVs*-TiO_{2-x}. (a) XRD patterns, (b) Raman spectra, (c) optical band gaps, (d) EPR spectra, (e) high-resolution XPS spectra at Ti 2p regions, and (f) valence band XPS spectra of wrinkled TiO_2 and *OVs*-TiO_{2-x}.

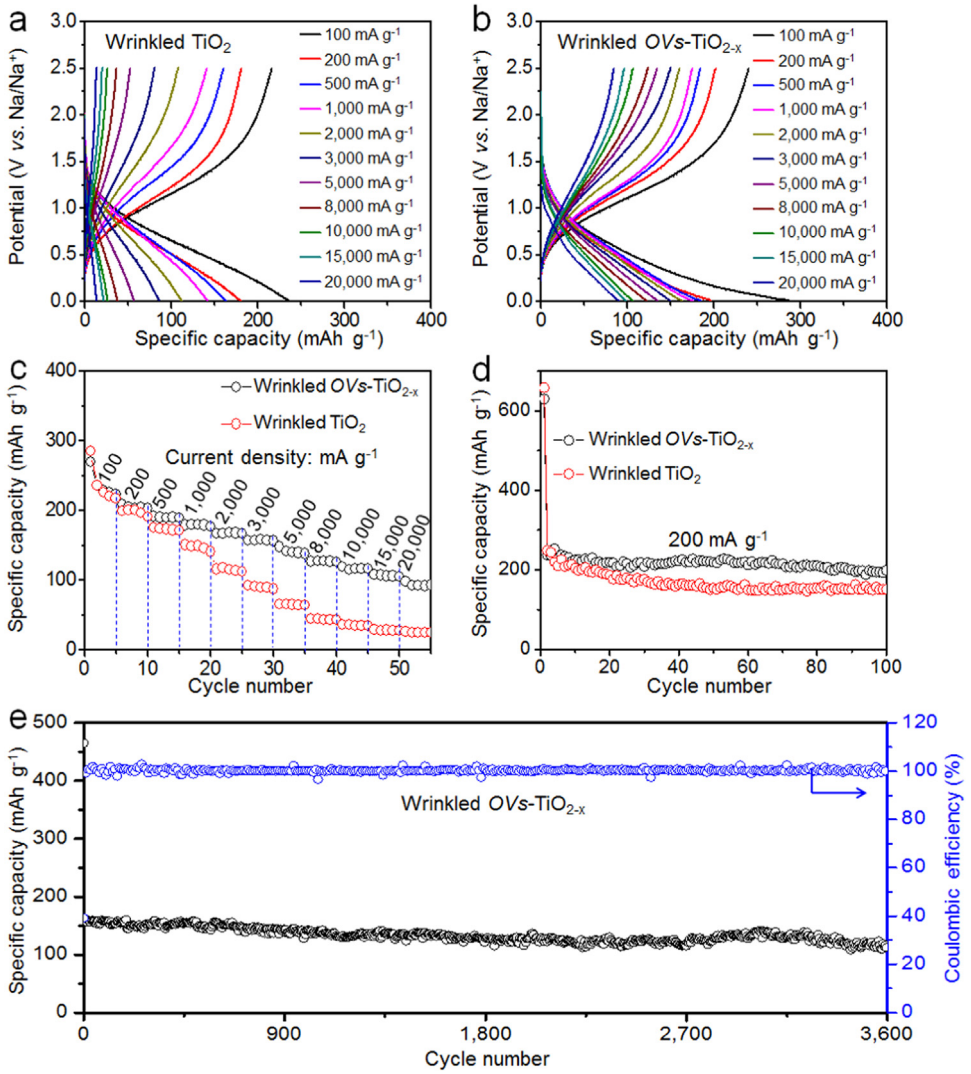

Fig. 3. Electrochemical performances of wrinkled TiO_2 and *OVs*-TiO_{2-x} as anode materials for SIBs. Galvanostatic charge/discharge profiles of (a) wrinkled TiO_2 and (b) *OVs*-TiO_{2-x} under various current rates. (c) Rate performances and (d) cycling performances of wrinkled TiO_2 and *OVs*-TiO_{2-x}. (e) Long-term cycling performance and corresponding Coulombic efficiencies of wrinkled *OVs*-TiO_{2-x} at 2000 mA g^{-1}.

peak at 458.0 eV was deconvoluted into two Gaussian peaks at 457.3 eV (Ti^{3+}) and 458.0 eV (Ti^{4+}), respectively (Fig. S7). The atomic ratio of Ti^{3+}:Ti^{4+} was calculated to be 11.9:88.1 for the outermost surface, thus the proportion of Ti and O can be noted as $TiO_{1.96}$. The valence band XPS spectrum of wrinkled TiO_2 (Fig. 2f) displays the typical characteristics of anatase TiO_2, with the edge of the maximum energy level at about 2.12 eV; While the valence band maximum of wrinkled *OVs*-TiO_{2-x} shifts to 1.55 eV, indicating the efficient band engineering. The results confirm that the formation of Ti^{3+} induces the changes in optical absorption, chemical status and band structure.

To evaluate the sodium storage performances of wrinkled TiO_2 and *OVs*-TiO_{2-x}, cyclic voltammograms (CV) were measured in the potential range of 0.01–2.5 V *vs.* Na/Na^+ at 0.2 mV s^{-1} (Fig. S8). For wrinkled *OVs*-TiO_{2-x}, an irreversible reduction peak appeared at 0.71 V in the 1st cathodic cycle, which was ascribed to the formation of solid electrolyte interphase (SEI) film caused by the decomposition of electrolyte [47]. Subsequently, the reduction peak disappeared and the SEI film became stable in the following cycles. At the end of the 1st cathodic cycle, a sharp peak caused by the disproportion reaction and the formation of Ti° was observed at 0.10 V [31]. In the 2nd cycle, a pair of peaks at 0.69 V (cathodic) and 0.87 V (anodic) appeared, and then kept stable in the following cycles. These two peaks are related to the reversible Na^+ insertion/extraction in the host structure of wrinkled *OVs*-TiO_{2-x}, accompanying with the redox reactions of Ti^{4+}/Ti^{3+} [48].

High rate operation is very critical to SIBs, because of the Na^+ insertion/extraction in the host material is usually hindered by slow kinetics. Distinctively, wrinkled *OVs*-TiO_{2-x} exhibit impressively fast kinetics and ultrahigh rate capability. Fig. 3a and b show the galvanostatic charge/discharge profiles of wrinkled TiO_2 and *OVs*-TiO_{2-x} under increasing current rates. As a control sample, the charge/discharge curves of wrinkled TiO_2 deformed above 5000 mA g^{-1}, and delivered a discharge capacity of 17 mAh g^{-1} at 20,000 mA g^{-1} (Fig. 3a). In contrast, the galvanostatic charge/discharge curves of wrinkled *OVs*-TiO_{2-x} retained good shapes under high current rates, and the discharge capacity maintains at 91 mAh g^{-1} even under 20,000 mA g^{-1} (Fig. 3b). This result indicates that the Na^+ insertion and extraction in wrinkled *OVs*-TiO_{2-x} are much easier than that in wrinkled TiO_2 [25]. Fig. 3c compares the rate performances of wrinkled TiO_2 and *OVs*-TiO_{2-x}, confirming the significantly enhanced rate capability of wrinkled *OVs*-TiO_{2-x}. In detail, the discharge capacities of wrinkled TiO_2 at 100, 200, 500, 1000, 2000, 3000, 5000, 8000, 10,000, 15,000 and 20,000 mA g^{-1} are 212, 190, 161, 140, 107, 81, 56, 35, 27, 20 and 17 mAh g^{-1}, respectively; while the discharge capacities of wrinkled *OVs*-TiO_{2-x} increase to 224, 208, 188, 176, 165, 157, 140, 128, 116, 103 and 91 mAh g^{-1}, respectively. The significantly-improved rate capability of wrinkled *OVs*-TiO_{2-x} should be ascribed to the high

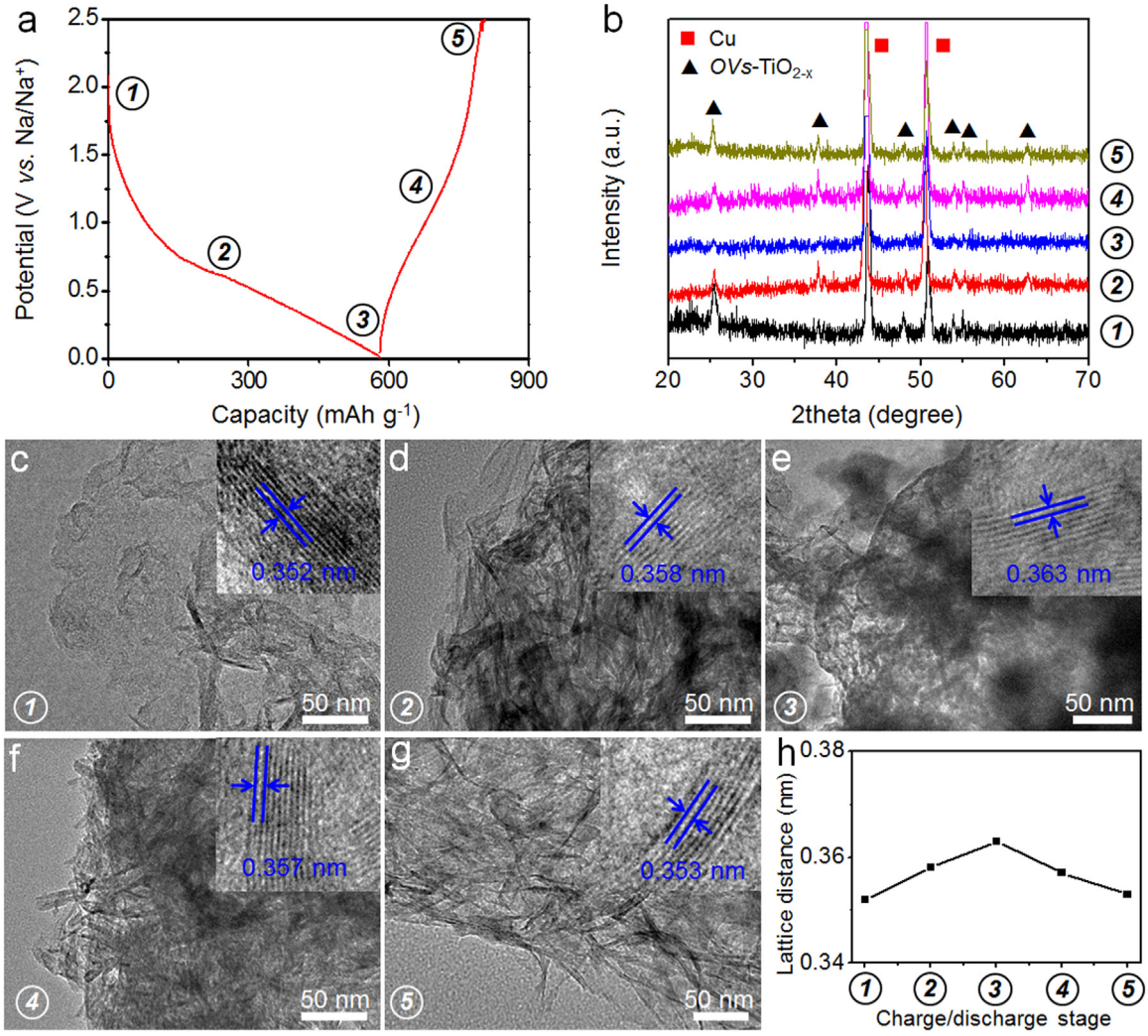

Fig. 4. Compositional and structural characterizations of wrinkled *OVs*-TiO_{2-x} during Na^+ insertion/extraction processes. (a) The initial galvanostatic charge/discharge profiles of wrinkled *OVs*-TiO_{2-x}. (b) *Ex-situ* XRD patterns of wrinkled *OVs*-TiO_{2-x} at different charge/discharge stages. (c–g) *Ex-situ* TEM images of wrinkled *OVs*-TiO_{2-x} at different charge/discharge stages: (c) stage *1*, (d) stage *2*, (e) stage *3*, (f) stage *4*, and (g) stage *5*. The insets in (c–g) show the corresponding HRTEM images. (h) Lattice distances of wrinkled *OVs*-TiO_{2-x} at different charge/discharge stages.

electrical conductivity originated from Ti^{3+} species and abundant oxygen vacancies, which can efficiently promote the electron transfer during Na^+ insertion/extraction processes. The wrinkled *OVs*-TiO_{2-x} exhibit remarkable rate performance among the existing TiO_2-based anode materials in literatures [26–30,48,49], suggesting the great potential for future applications in SIBs.

The cycling performances of wrinkled TiO_2 and *OVs*-TiO_{2-x} were also compared. At the current rate of 200 mA g^{-1}, wrinkled *OVs*-TiO_{2-x} delivers better cycling stability and higher discharge capacities than those of wrinkled TiO_2 (Fig. 3d). The initial discharge and charge capacities of wrinkled *OVs*-TiO_{2-x} were 649 and 226 mAh g^{-1}, respectively. The corresponding Coulombic efficiency in the 1st cycle is 40%, which is normal for TiO_2-based anode materials. The low initial Coulombic efficiency should be attributed to the presence of some irreversible capacity caused by the formation of sodium titanate with poor electrical conductivity, which resulted in the increase of interfacial resistances and energy barriers for Na^+ insertion/extraction [48]. The discharge capacity in the 2nd cycle was 222 mAh g^{-1}, then it kept very stable and finally reached a high value of 201 mAh g^{-1} in the 100th cycle. The capacity retention was ~ 91% corresponding to the capacity of the 2nd cycle. In contrast, the wrinkled TiO_2 delivered a lower discharge capacity (151 mAh g^{-1}) in the 100th cycle, and the capacity retention was ~ 61% relative to the 2nd cycle. Moreover, the Coulombic efficiency of wrinkled TiO_2 electrode is comparable to that of wrinkled *OVs*-TiO_{2-x} electrode, as shown in Fig. S9. The resistance characteristics of wrinkled TiO_2 and *OVs*-TiO_{2-x} electrodes after cycling were investigated. As shown in Fig. S10, both wrinkled TiO_2 and *OVs*-TiO_{2-x} electrodes exhibited slightly higher resistances than those before cycling, while the resistance of wrinkled *OVs*-TiO_{2-x} electrode after cycling is still much smaller than that of wrinkled TiO_2 electrode. To better evaluate the long-term cycling performance, the wrinkled *OVs*-TiO_{2-x} based anode was charge/discharged for 3600 cycles under a high current rate of 2000 mA g^{-1} (Fig. 3e). The initial discharge and charge capacities of wrinkled *OVs*-TiO_{2-x} were 465 and 182 mAh g^{-1}; the discharge capacity in the 2nd cycle was 172 mAh g^{-1}, and then it retained at 112 mAh g^{-1} after testing for 3,600 cycles. This corresponds to a low capacity decay of only 0.01% per cycle from the 2nd cycle to the 3600th cycle, indicating the high capacity retention capability and ultra-stable cycling performance of wrinkled *OVs*-TiO_{2-x}. Compared with $Na_2Ti_3O_7$ based anode as a control sample (Fig. S11 and S12), the wrinkled *OVs*-TiO_{2-x} shows much superior performances in terms of discharge capacity, rate performance and long-term cycling capability.

To further investigate the sodium storage mechanism, the phase changes of wrinkled *OVs*-TiO_{2-x} upon cycling were analyzed by *ex-situ* XRD (Fig. 4a and b). At the stage *1*, the XRD pattern displayed the typical peaks of pristine wrinkled *OVs*-TiO_{2-x}. Subsequently, the

diffraction peaks became weaker at the stage *2*, and then almost vanished at the stage *3*. This may be attributed to the formation of amorphous sodium titanate structure upon Na^+ insertion [30]. When charged back to 1.0 V (stage *4*) and then 2.5 V (stage *5*), the diffraction peak intensities gradually increased again, indicating the gradual removal of Na^+ ions and the recovery of crystallinity. Moreover, *Ex-situ* TEM and HRTEM characterizations were performed to further examine the structure variations of wrinkled *OVs*-TiO_{2-x} during Na^+ insertion and extraction processes. As shown in Fig. 4c, the original lattice distances at stage *1* is about 0.352 nm, corresponding to the (101) planes of wrinkled *OVs*-TiO_{2-x}. However, at stage *2* and *3*, the lattice distances expand to about 0.358 and 0.363 nm, respectively (Fig. 4d, e), probably due to the large Na^+ ion insertion into wrinkled *OVs*-TiO_{2-x} structures. At stage *4* and *5*, the observed lattice distances of wrinkled *OVs*-TiO_{2-x} recover to 0.357 and 0.353 nm, respectively (Fig. 4f, g). Thus, the lattice distance of wrinkled *OVs*-TiO_{2-x} increases at the charge stages and decreases at the discharge stages (Fig. 4h), indicating a reversible variation of the lattice parameters resulted from the repeating Na^+ insertion/extraction. Combining with the results of CV curves (Fig. S8) and galvanostatic charge/discharge profiles (Fig. 3b), it is concluded that the capacity of wrinkled *OVs*-TiO_{2-x} in SIBs mainly originates from the redox reactions of Ti^{4+}/Ti^{3+} and the Na^+ insertion/extraction. The possible mechanism for the high sodium storage performance of wrinkled *OVs*-TiO_{2-x} electrode can be attributed to the following aspects [30,37,43,50]: (1) The electrical conductivity of wrinkled *OVs*-TiO_{2-x} has been significantly improved because of the introduction of abundant oxygen vacancies, which can ensure fast electron transfer; (2) The wrinkled structure can significantly reduce the Na^+ diffusion length, and the conductive networks formed by wrinkled *OVs*-TiO_{2-x} can facilitate the electron transfer during Na^+ insertion/extraction processes; (3) The abundant oxygen vacancies can induce the enlarged lattice spacing of wrinkled *OVs*-TiO_{2-x}, enabling the fast kinetics of sodiation/desodiation.

4. Conclusions

In summary, we found that wrinkled *OVs*-TiO_{2-x} nanosheets can serve as a promising anode material for SIBs. The sodium storage performance of wrinkled *OVs*-TiO_{2-x} is originated from the Ti^{4+}/Ti^{3+} redox reactions accompanying with the reversible Na^+ insertion/extraction into/from the wrinkled *OVs*-TiO_{2-x} structure. By incorporating the Ti^{3+} species and abundant oxygen vacancies, the wrinkled *OVs*-TiO_{2-x} exhibited greatly improved electrical conductivity and sodium storage capability than pristine TiO_2. When used in SIBs, the wrinkled *OVs*-TiO_{2-x} can deliver outstanding rate capability and ultra-long cycling stability. This study provides new insights into the design of defect-engineered electrode materials for non-lithium ion secondary batteries with ultrafast charge/discharge rates and ultrahigh cycling stability.

Acknowledgements

This work is supported by National Key R&D Program of China (2017YFA0208200, 2016YFB0700600, 2015CB659300), Projects of NSFC (21403105, 21573108), Natural Science Foundation of Jiangsu Province (BK20150583, BK20170644), and the Fundamental Research Funds for the Central Universities (020514380107).

Appendix A. Supporting information

Supplementary data associated with this article can be found in the online version at doi:10.1016/j.nanoen.2018.08.043.

References

[1] N. Yabuuchi, K. Kubota, M. Dahbi, S. Komaba, Chem. Rev. 114 (2014) 11636–11682.
[2] M.D. Slater, D.H. Kim, E.J. Lee, C.S. Johnson, Adv. Funct. Mater. 23 (2013) 947–958.
[3] V. Palomares, P. Serras, I. Villauenga, K.B. Hueso, J. Carretero-Gonzalez, T. Rojo, Energy Environ. Sci. 5 (2012) 5884–5901.
[4] H.L. Pan, Y.S. Hu, L.Q. Chen, Energy Environ. Sci. 6 (2012) 2338–2360.
[5] S.P. Ong, V.L. Chevrier, G. Hautier, A. Jain, C. Moore, S. Kim, X.H. Ma, G. Ceder, Energy Environ. Sci. 4 (2011) 3680–3688.
[6] V. Palomares, M. Casas-Cabanas, E. Castillo-Martinez, M.H. Han, T. Rojo, Energy Environ. Sci. 6 (2013) 2312–2337.
[7] V.L. Cherier, G. Ceder, J. Electrochem. Soc. 158 (2011) A1011–A1014.
[8] M.S. Islam, C.A.J. Fisher, Chem. Soc. Rev. 43 (2014) 185–204.
[9] Y. Liu, N. Zhang, L. Jiao, J. Chen, Adv. Mater. 27 (2015) 6702–6707.
[10] Z. Zhang, J. Zhang, X. Zhao, F. Yang, Carbon 95 (2015) 552–559.
[11] Y.H. Xu, Y.J. Zhu, Y.H. Liu, C.S. Wang, Adv. Energy Mater. 3 (2013) 128–133.
[12] Y.C. Liu, N. Zhang, L.F. Jiao, Z.L. Tao, J. Chen, Adv. Funct. Mater. 25 (2015) 214–220.
[13] J. Liu, L.T. Yu, C. Wu, Y.R. Wen, K.B. Yin, F.K. Chiang, R.Z. Hu, J.W. Liu, L.T. Sun, L. Gu, J. Maier, Y. Yu, M. Zhu, Nano Lett. 17 (2017) 2034–2042.
[14] W.H. Li, S.H. Hu, X.Y. Luo, Z.L. Li, X.Z. Sun, M.S. Li, F.F. Liu, Y. Yu, Adv. Mater. 29 (2017) 1605820.
[15] X.L. Fan, J.F. Mao, Y.J. Zhu, C. Luo, L.M. Suo, T. Gao, F.D. Han, S.C. Liou, C.S. Wang, Adv. Energy Mater. 5 (2015) 1500174.
[16] K. Gotoh, T. Ishikawa, S. Shimadzu, N. Yabuuchi, S. Komaba, K. Takeda, A. Goto, K. Deguchi, S. Ohki, K. Hashi, T. Shimizu, H. Ishida, J. Power Sources 225 (2013) 137–140.
[17] S. Komaba, W. Murata, T. Ishikawa, N. Yabuuchi, T. Ozeki, T. Nakayama, A. Ogata, K. Gotoh, K. Fujiwara, Adv. Funct. Mater. 21 (2011) 3859–3867.
[18] C. Bommier, W. Luo, W.Y. Gao, A. Greaney, S. Ma, X. Ji, Carbon 76 (2014) 165–174.
[19] J.Y. Hwang, S.T. Myung, J.H. Lee, A. Abouimrane, L. Belharouak, Y.K. Sun, Nano Energy 16 (2015) 218–226.
[20] D. Li, L. Zhang, H. Chen, J. Wang, L.X. Ding, S. Wang, P.J. Ashman, H. Wang, J. Mater. Chem. A 4 (2016) 8630–8635.
[21] V.G. Pol, E. Lee, D. Zhoua, F. Dogana, J.M. Calderon-Morenob, C.S. Johnson, Electrochim. Acta 127 (2014) 61–67.
[22] D.H. Wang, D.W. Choi, J. Li, Z.G. Yang, Z.M. Nie, R. Kou, D.H. Hu, C.M. Wang, L.V. Saraf, J.G. Zhang, L.A. Aksay, J. Liu, ACS Nano 3 (2009) 907–914.
[23] J.S. Chen, Y.L. Tan, C.M. Li, Y.L. Cheah, D.Y. Luan, S. Madhavi, F.Y.C. Boey, L.A. Archer, X.W. Lou, J. Am. Chem. Soc. 132 (2010) 6124–6130.
[24] A.R. Armstrong, G. Armstrong, J. Canales, R. Garcia, P.G. Bruce, Adv. Mater. 17 (2005) 862–865.
[25] D.W. Su, S.X. Dou, G.X. Wang, Chem. Mater. 27 (2015) 6022–6029.
[26] H. Xiong, M.D. Slater, M. Balasubramanian, C.S. Johnson, T. Rajh, J. Phys. Chem. Lett. 2 (2011) 2560–2565.
[27] Y. Xu, E.M. Lotfabad, H. Wang, B. Farbod, Z. Xu, A. Kohandehghanab, D. Mitlin, Chem. Commun. 49 (2013) 8973–8975.
[28] Y.C. Yang, X.B. Ji, M.J. Jing, H.S. Hou, Y.R. Zhu, L.B. Fang, X.M. Yang, Q.Y. Chen, C.E. Banks, J. Mater. Chem. A 3 (2015) 5648–5655.
[29] L. Wu, D. Buchholz, D. Bresser, L.G. Chagas, S. Passerini, J. Power Sources 251 (2014) 379–385.
[30] K.T. Kim, G. Ali, K.Y. Chung, C.S. Yoon, H. Yashiro, Y.K. Sun, J. Lu, K. Amine, S.T. Myung, Nano Lett. 14 (2014) 416–422.
[31] L.M. Wu, D. Bresser, D. Buchhloz, G.A. Giffin, C.R. Castro, A. Ochel, S. Passerini, Adv. Energy Mater. 5 (2015) 1401142.
[32] S.T. Myung, M. Kikuchi, C.S. Yoon, H. Yashiro, S.J. Kim, Y.K. Sun, B. Scrosati, Energy Environ. Sci. 6 (2013) 2609–2614.
[33] K.S. Han, J.W. Lee, Y.M. Kang, J.Y. Lee, J.K. Kang, Small 4 (2008) 1682–1686.
[34] K. Szot, M. Rogala, W. Speier, Z. Klusek, A. Besmehn, R. Waser, Nanotechnology 22 (2011) 254001.
[35] X.Y. Liu, G.L. Zhu, X. Wang, X.T. Yuan, T.Q. Lin, F.Q. Fu, Adv. Energy Mater. 6 (2016) 1600452.
[36] X.B. Chen, L. Liu, F.Q. Huang, Chem. Soc. Rev. 44 (2015) 1861–1885.
[37] Y. Zhang, Z.Y. Ding, C.W. Foster, C.E. Banks, X.Q. Qiu, X.B. Ji, Adv. Funct. Mater. 27 (2017) 1700856.
[38] S.T. Myung, N. Takahashi, S. Komaba, C.S. Yoon, Y.K. Sun, K. Amine, H. Yashiro, Adv. Funct. Mater. 21 (2011) 3231–3241.
[39] H.Q. Tan, Z. Zhao, M. Niu, C.Y. Mao, D.P. Cao, D.J. Cheng, P.Y. Feng, Z.C. Sun, Nanoscale 6 (2014) 10216–10223.
[40] W. Zhou, W. Li, J.Q. Wang, Y. Qu, Y. Yang, Y. Xie, K.F. Zhang, L. Wang, H.G. Fu, D.Y. Zhao, J. Am. Chem. Soc. 136 (2014) 9280–9283.
[41] Z. Wang, C.Y. Yang, T.Q. Lin, H. Yin, P. Chen, D.Y. Wan, F.F. Xu, F.Q. Huang, J.H. Lin, X.M. Xie, M.H. Jiang, Adv. Funct. Mater. 23 (2013) 5444–5450.
[42] Z. Wang, C.Y. Yang, T.Q. Lin, H. Yin, P. Chen, D.Y. Wan, F.F. Xu, F.Q. Huang, J.H. Lin, X.M. Xie, M.H. Jiang, Energy Environ. Sci. 6 (2013) 3007–3014.
[43] C.J. Chen, Y.W. Wen, X.L. Hu, X.L. Ji, M.Y. Yan, L.Q. Mai, P. Hu, B. Shan, Y.H. Huang, Nat. Commun. 6 (2015) 6929.
[44] V. Etacheri, J.E. Yourey, B.M. Bartlett, ACS Nano 8 (2014) 1491–1499.
[45] T.Q. Lin, C.Y. Yang, Z. Wang, H. Yin, X.J. Lu, F.Q. Huang, J.H. Lin, X.M. Xie, M.H. Jiang, Energy Environ. Sci. 7 (2014) 967–972.
[46] F. Zuo, K. Bozhilov, R.J. Dillon, L. Wang, P. Smith, X. Zhao, C. Bardeen, P. Feng, Angew. Chem. Int. Ed. 51 (2012) 6223–6226.
[47] Y. Yeo, J.W. Jung, K. Park, I.D. Kim, Sci. Rep. 5 (2015) 13862.
[48] A. Shoaib, Y.X. Huang, J. Liu, J.J. Liu, M. Xu, Z.H. Wang, R.J. Chen, J.T. Zhang, F. Wu, J. Power Sources 342 (2017) 405–413.
[49] Y. Zhang, C.W. Wang, H.S. Hou, G.Q. Zou, X.B. Ji, Adv. Energy Mater. 2 (2016) 1600173.
[50] J. Chen, W.X. Song, H.S. Hou, Y. Zhang, M.J. Jing, X.N. Jia, X.B. Ji, Adv. Funct. Mater. 25 (2015) 6793–6801.